International Journal of Heat and Mass Transfer 147 (2020) 118934

Contents lists available at ScienceDirect

International Journal of Heat and Mass Transfer

journal homepage: www.elsevier.com/locate/ijhmt

Free-surface flow of confined volatile simple fluids driven by a horizontal temperature gradient: From a comprehensive numerical model to a simplified analytical description

Tongran Qin [a,*], Roman O. Grigoriev [b]

[a] The Wallace H. Coulter Department of Biomedical Engineering, Georgia Institute of Technology, Atlanta, GA 30332, USA
[b] School of Physics, Georgia Institute of Technology, Atlanta, GA 30332, USA

ARTICLE INFO

Article history:
Received 17 July 2019
Received in revised form 20 September 2019
Accepted 21 October 2019
Available online 31 October 2019

Keywords:
Marangoni convection
Two-phase flows
Free surface flows
Phase change
Heat pipes
Thermocapillary flows

ABSTRACT

We study the flow in a confined layer of volatile simple liquid subjected to a horizontal temperature gradient. The somewhat unusual feature of this problem is that the gas layer, which contains a mixture of vapor and air, plays a very important role. Due to phase change occurring at the free surface, the mean flow in the liquid layer and its stability are controlled almost entirely by the mass and heat transport in the gas phase. To explain why this is the case, we use numericae simulations based on a comprehensive two-sided transport model to motivate a simplified analytical description of transport in the gas phase for high-aspect-ratio geometries. This simplified description allows us to compute the interfacial temperature and hence the thermocapillary stresses at the free surface which control the flow in the central region of the cavity and to predict the net heat and mass flux in the direction of the applied gradient. The analytical solutions are found to agree quite well with the results of our numerical simulations as well as the results of relevant previous studies.

1. Introduction

The problem of convection in volatile fluids with a free surface subject to horizontal temperature gradient has received a lot of attention due to the increasing demand for more efficient and compact cooling technologies. In particular, two-phase evaporative cooling technologies achieve high heat fluxes by exploiting large latent heat associated with phase change at the liquid-gas interface. Thermal management devices such as heat pipes, thermosyphons, and heat spreaders are typically sealed (to avoid loss of working fluid due to evaporation), with a layer of liquid in contact with a layer of gas mixture containing the vapor and the noncondensable gases (such as air) [1]. Under terrestrial conditions, horizontal temperature gradient generates a convective two-phase flow which is driven primarily by a combination of capillary force, thermocapillary stresses, and – for larger devices – buoyancy.

While noncondensable gases are well-known to impede phase change and reduce heat transfer coefficient associated with condensation [2], it is usually infeasible to remove them completely from the gas phase, as air tends to dissolve in liquids and be absorbed in solids. Therefore, a fundamental understanding of two-phase flows and heat and mass transfer with varying levels of noncondensables is essential for better design of evaporative cooling devices. However, our current understanding of this problem remains incomplete (a detailed review of the state-of-art in the field and various open questions can be found in Ref. [3]). A key observation is that the design of thermal management devices to this day is based on experimental studies of buoyancy-thermocapillary convection, the vast majority of which have been performed at ambient (atmospheric) conditions, while the ideal operating conditions correspond to the gas phase dominated by the vapor. For instance, many theoretical studies [4–13] focus on the liquid layer and ignore transport in the gas layer, which is only justified at atmospheric conditions, so their results are of limited value where they matter the most. Only a few theoretical studies have used comprehensive models which described momentum, heat, and mass flux in both liquid and gas phase, as well as a detailed description of phase change at their interface [14–17]. Yet, without such detailed models it is impossible to correctly identify the limiting factors affecting the performance of evaporative cooling devices or construct simplified models that could be used to build intuition about the key design principles.

Several existing two-sided transport models for two-phase flow of volatile fluids driven by horizontal temperature gradients in the

* Corresponding author.
E-mail address: tongran@gatech.edu (T. Qin).

https://doi.org/10.1016/j.ijheatmasstransfer.2019.118934
0017-9310/

presence of noncondensables include all four basic components of this problem: (1) the fluid flow and the heat transport in the liquid phase, (2) the fluid flow, and the heat and mass transport in the gas phase, (3) the dynamics at the interface between the two phases (*e.g.* the heat and mass transport across the interface), and (4) the heat conduction within the solid walls of the cavity containing the working fluid. While these models provide a comprehensive description of two-phase flows, they are only valid in the limiting cases when the gas phase is dominated by either air [14,16] or vapor [17,18] and cannot accurately describe intermediate compositions. Here we present a more general transport model valid for arbitrary composition of the gas phase, which can only be solved numerically. Furthermore, to gain the insight into the numerical solutions, we derive a greatly simplified transport model, which can be solved analytically.

The outline of the present study is as follows: The comprehensive model is described in detail in Section 2. The results of the numerical investigation of this model are analyzed in Section 3. The simplified model is derived and its predictions are compared with those of the comprehensive numerical model in Section 4. Finally, our summary and conclusions are presented in Section 5.

2. Comprehensive transport model

2.1. Governing equations

The generalized two-sided model of two-phase flow of non-isothermal volatile fluids presented below is loosely based on the previous models valid in the limiting cases where the gas phase is dominated by either air [16] or vapor [19,17]. In those models, mass transport was described using the advection-diffusion equation for the mass density of the dilute component. The present model describes mass transport in terms of the molar fraction, which makes it applicable over the entire range of composition. Specifically, local mass conservation for the vapor can be written in terms of its number density n_v

$$\partial_t n_v + \nabla \cdot \mathbf{j}_v = 0, \tag{1}$$

where the number density of vapor n_v can be related to the total number density n_g through the vapor concentration (molar fraction) c_v

$$n_v = c_v n_g, \tag{2}$$

and $\mathbf{j}_v$ is the total number flux of vapor

$$\mathbf{j}_v = n_v \mathbf{u} - \mathbf{j}'_v, \tag{3}$$

which consists of two components: the first term on the right-hand-side represents the advection due to the gas mixture flowing with the average speed $\mathbf{u}$ and the second term – the molecular diffusion component. The diffusion number flux $\mathbf{j}'_v$ is driven by the concentration gradient, which can be described using the Maxwell-Stefan relation [20]. For a binary mixture, this relation essentially reduces to Fick's law

$$\mathbf{j}'_v = -n_g D \nabla c_v, \tag{4}$$

where the binary mass diffusivity D is a function of pressure p_g and temperature T

$$D = D_0 \frac{p_g^0}{p_g} \left(\frac{T}{T_0}\right)^{3/2}. \tag{5}$$

Here and below we use the index 0 to denote the reference (equilibrium) values which correspond to $\Delta T = 0$. With the help of (2)–(4) we find

$$\partial_t (c_v n_g) + \nabla \cdot (c_v n_g \mathbf{u}) = \nabla \cdot (n_g D \nabla c_v). \tag{6}$$

Note that, in this study, we are ignoring the thermodiffusion (Soret) and diffusion-thermo (Dufour) effects, which are typically negligible and trivial to take into account.

Both the vapor and air are assumed ideal, hence the total number density n_g can be computed using the ideal gas law

$$n_g = \frac{p_g}{k_B T}, \tag{7}$$

where p_g is the total pressure in the gas phase and k_B is the Boltzman constant. The corresponding chemical potential is

$$\mu_g = \mu_g^0 + RT \ln \frac{p_g}{p_g^0}, \tag{8}$$

where R is the universal gas constant. The constancy of the chemical potential implies that the gas pressure is constant (even taking viscous effects into account this remains an excellent approximation [19]). Since the gas is non-isothermal, the flow cannot be considered incompressible. The conservation law for the total number density is

$$\partial_t n_g + \nabla \cdot (n_g \mathbf{u}) = 0. \tag{9}$$

Combining (6) and (9) we find

$$\partial_t c_v + \mathbf{u} \cdot \nabla c_v = n_g^{-1} \nabla \cdot (n_g D \nabla c_v). \tag{10}$$

Since the product $n_g D \propto T^{1/2}$ depends rather weakly on the temperature (and hence on the position), we consider it constant, yielding an advection-diffusion equation for the concentration of vapor

$$\partial_t c_v + \mathbf{u} \cdot \nabla c_v = D \nabla^2 c_v. \tag{11}$$

The transport Eq. (11) is valid for the entire range of gas composition. Although a similar equation can be written for air, its concentration $c_a = n_a / n_g$ can instead be found from

$$c_v + c_a = 1. \tag{12}$$

The transport equations for momentum, temperature, and mass (in the liquid phase) are standard and remain the same as in the previous models [16,17]. The momentum transport in the bulk is described by the Navier-Stokes equation

$$\rho(\partial_t \mathbf{u} + \mathbf{u} \cdot \nabla \mathbf{u}) = -\nabla p + \mu \nabla^2 \mathbf{u} + \rho \mathbf{g}, \tag{13}$$

where ρ and μ are the fluid's density and viscosity, respectively, and $\mathbf{g}$ is the gravitational acceleration. Following standard practice, the Boussinesq approximation is used, where the density variation due to temperature and concentration is only considered in the last term on the right-hand-side, which represents the buoyancy force. In the liquid phase,

$$\rho_l = \rho_l^0 [1 - \beta_l (T - T_0)], \tag{14}$$

where $\beta_l = -(\partial \rho_l / \partial T)/\rho_l$ is the coefficient of thermal expansion. In the gas phase,

$$\rho_g = \rho_a + \rho_v = (m_a^1 c_a + m_v^1 c_v) n_g, \tag{15}$$

where m_a^1 and m_v^1 are the masses of the air and vapor molecules. On the left-hand-side of (13) the density is considered constant for each phase, and is taken to be equal to the spatial average of the fields given by (14) or (15). The liquid phase is considered incompressible, since β_l is small, so that

$$\nabla \cdot \mathbf{u} = 0. \tag{16}$$

For the gas phase, in steady state, we find from (7) and (9)

$$\nabla \cdot \mathbf{u} = -n_g^{-1} \mathbf{u} \cdot \nabla n_g = T^{-1} \mathbf{u} \cdot \nabla T, \tag{17}$$

where the right-hand-side can also be neglected for small temperature gradients considered here (e.g., an applied temperature differ-

ence of $\Delta T = 10$ K corresponds to about 1% variation in the temperature along the interface [16]). Finally, the heat transport in the bulk is described by the advection–diffusion equation

$$\partial_t T + \mathbf{u}\cdot\nabla T = \alpha\nabla^2 T, \tag{18}$$

where $\alpha = k/\rho C_p$ is the thermal diffusivity, k is the thermal conductivity, and C_p is the specific heat capacity, of the fluid.

For a volatile fluid in a sealed cavity, the external temperature gradient causes both evaporation and condensation, which leads to movement of the liquid-gas interface, and the change of the volumes of the two phases. In a numerical implementation of the model, the change in the liquid volume does not satisfy the mass flux balance at the interface exactly due to numerical errors (e.g., discretization). These errors eventually accumulate, leading to a loss off mass conservation for the liquid phase and resulting, due to the large ratio of the densities, in a large relative error for the mass of vapor, unless corrected. The approximations made in deriving the mass transport Eq. (11) will also contribute to the error. To ensure global mass/number conservation for each component (vapor and air) we will require

$$\int_{\text{liquid}} n_l\, dV + \int_{\text{gas}} c_v n_g\, dV = N_v = \frac{m_v}{m_v^1} \tag{19}$$

and

$$\int_{\text{gas}} (1-c_v)\, n_g\, dV = N_a = \frac{m_a}{m_a^1}, \tag{20}$$

where N_v and N_a are the total numbers of molecules of the vapor and air, and m_v and m_a are the initial net mass of vapor and air. A (spatially uniform) pressure offset p_o and vapor concentration correction Δc_v are introduced to enforce these conservation laws. They are updated at each time step by solving the constrains (19) and (20) with

$$\begin{aligned} c_v &= c_v' + \Delta c_v, \\ p_g &= p + p_o, \end{aligned} \tag{21}$$

where c_v' is the (uncorrected) numerical solution of the transport Eq. (11), p_g is the absolute pressure, and p is the dynamic pressure in the gas phase obtained by solving the momentum transport (13) and incompressibility Eq. (16).

2.2. Boundary conditions

The system of coupled evolution Eqs. (16), (13), (18), and (11) for the velocity, pressure, temperature, and concentration fields should be solved in a self-consistent manner, subject to the boundary conditions describing the balance of momentum, heat, and mass/number fluxes. In the comprehensive model, we will describe phase equilibrium using the Antoine equation, which is valid over a wide range of conditions,

$$\ln p_v = A_v - \frac{B_v}{C_v + T}, \tag{22}$$

where A_v, B_v, and C_v are empirical coefficients. In the simplified description, it will be more convenient to use the more popular Clausius-Clapeyron equation

$$\ln\frac{p_v}{p_v^0} = -\frac{\mathscr{L}}{\overline{R}_v}\left(\frac{1}{T} - \frac{1}{T_0}\right), \tag{23}$$

where $\overline{R}_v$ is the specific gas constant for vapor. The Clausius–Clapeyron equation and the Antoine equation are equivalent for small deviations from T_0 when the latent heat is defined according to

$$\mathscr{L} = \frac{B_v \overline{R}_v T_0^2}{(C_v + T_0)^2}, \tag{24}$$

as can be verified by evaluating the relations (22) and (23) and their partial derivatives with respect to T at T_0. In the following, these relations will be used to define the saturation temperature T_s in terms of the partial pressure p_v.

We will rely on the kinetic theory of gases [21] which assumes that the chemical potential and the temperature are continuous across the liquid-gas interface

$$T_l = T_i = T_g, \tag{25}$$

yielding the following expression for the number density flux across the interface due to phase change

$$j_v = \frac{2\lambda}{2-\lambda} n_g c_v \sqrt{\frac{\overline{R_v T_i}}{2\pi}}\left[\frac{p_l - p_g}{\rho_l R_v T_i} + \frac{\mathscr{L}}{R_v T_i}\frac{T_i - T_s}{T_s}\right], \tag{26}$$

where λ is the accommodation coefficient and T_s is computed from (22). For nonpolar liquids, the accommodation coefficient is found to be equal (or very close) to unity [22,23], so we set $\lambda = 1$ in this study.

The mass/number flux balance for the vapor on the gas side of the interface is given by

$$j_v = n_g c_v \hat{\mathbf{n}}\cdot(\mathbf{u}_g - \mathbf{u}_i) - n_g D\,\partial_n c_v, \tag{27}$$

where $\mathbf{u}_i$ is the velocity of the interface, $\hat{\mathbf{n}}$ is the surface normal vector, and $\partial_n = \hat{\mathbf{n}}\cdot\nabla$. Since air is noncondensable, its flux across the interface is zero:

$$0 = n_g c_a \hat{\mathbf{n}}\cdot(\mathbf{u}_g - \mathbf{u}_i) - n_g D\,\partial_n c_a. \tag{28}$$

Using (12), (27), and (28) we can find a pair of boundary conditions for $\mathbf{u}_g$ and c_v at the interface:

$$\hat{\mathbf{n}}\cdot(\mathbf{u}_g - \mathbf{u}_i) = \frac{j_v}{n_g}, \tag{29}$$

and

$$\partial_n c_v = -\frac{1-c_v}{D}\frac{j_v}{n_g}. \tag{30}$$

The mass/number flux balance on the liquid side of the interface is given by

$$\hat{\mathbf{n}}\cdot(\mathbf{u}_l - \mathbf{u}_i) = \frac{j_v}{n_l}, \tag{31}$$

where the right-hand-side can be effectively set to zero, since $n_l \gg n_g$. While the normal component of velocity is discontinuous at the interface in the presence of phase change, the tangential components of velocity are continuous:

$$(\mathbb{I} - \hat{\mathbf{n}}\hat{\mathbf{n}})\cdot(\mathbf{u}_l - \mathbf{u}_g) = 0. \tag{32}$$

The normal component of the stress balance at the interface

$$\hat{\mathbf{n}}\cdot(\boldsymbol{\Sigma}_l - \boldsymbol{\Sigma}_g)\cdot\hat{\mathbf{n}} = \sigma\kappa + J_v^2(\rho_l^{-1} - \rho_v^{-1}) \tag{33}$$

incorporates the capillary pressure and vapor recoil [24], where

$$\boldsymbol{\Sigma} = \mu\left[\nabla\mathbf{u} + (\nabla\mathbf{u})^T\right] - p\mathbb{I} \tag{34}$$

is the stress tensor and $J_v = m_v^1 j_v$ is the mass flux of vapor. The effect of vapor recoil is found to be negligible in this study. The tangential component of the stress balance

$$(\mathbb{I} - \hat{\mathbf{n}}\hat{\mathbf{n}})\cdot(\boldsymbol{\Sigma}_l - \boldsymbol{\Sigma}_g)\cdot\hat{\mathbf{n}} = \nabla_s\sigma \tag{35}$$

accounts for the thermocapillary effect, where

$$\nabla_s\sigma = -\gamma\nabla_s T_i, \tag{36}$$

$\gamma = -\partial\sigma/\partial T$ is the temperature coefficient of surface tension, and

$$\nabla_s = (\mathbb{I} - \hat{\mathbf{n}}\hat{\mathbf{n}}) \cdot \nabla \tag{37}$$

is the surface gradient. The heat flux balance across the interface is given by

$$\mathscr{L} J_v = k_g \partial_n T_g - k_l \partial_n T_l. \tag{38}$$

Finally let us discuss the boundary conditions at the inner surfaces of the cavity confining the fluid. Following the previous experimental [25] and numerical studies [16,17], we assume the fluid is contained in a rectangular test cell with inner dimensions $L \times W \times H$ (cf. Fig. 1) and thin walls of thickness δ_w and conductivity k_w. The left wall is cooled with constant temperature T_c imposed on the outer surface, while the right wall is heated with constant temperature $T_h > T_c$ imposed on the outer surface. Since the walls are thin, one-dimensional conduction (normal to the surface) is assumed through all the walls, yielding the following mixed boundary conditions on the inner surfaces of the side walls:

$$T|_{x=0} = T_c + k_\imath \frac{\delta_w}{k_w} \partial_n T, \tag{39}$$
$$T|_{x=L} = T_h + k_\imath \frac{\delta_w}{k_w} \partial_n T,$$

where $\hat{\mathbf{n}}$ is the wall-normal vector and $\imath = g$ ($\imath = l$) above (below) the contact line. The remaining walls of the cell are assumed to be in contact with air, which is a poor thermal conductor, and hence can be considered adiabatic:

$$\partial_n T = 0. \tag{40}$$

Standard no-slip boundary conditions $\mathbf{u} = 0$ for the velocity and no-flux boundary conditions for the concentration of vapor

$$\partial_n c_v = 0 \tag{41}$$

are imposed on all the inner surfaces of the walls.

2.3. Solution procedure and numerical implementation

The main ingredients of the mathematical model of two-phase flow described above are summarized in Fig. 2. The main difficulty in using this comprehensive model is that all the transport equations are coupled, e.g., the mass, heat, and momentum transport equations along with the mass conservation (incompressibility) condition in the gas phase have to be solved simultaneously to compute the velocity $\mathbf{u}_g$, pressure p_g, concentration c_v, and temperature T_g,. Moreover, the transport in the gas and liquid phase is also coupled through the boundary conditions which, in turn, depend on the solutions to the transport equations. This requires an iterative procedure that ensures that both the transport equations and the boundary conditions are satisfied at each instant in time.

The governing equations in both phases are discretized using finite volume method [26–28], and the motion of the liquid–gas interface is described using the moving mesh method [29,30].

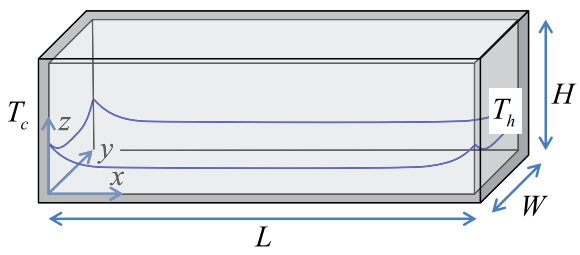

Fig. 1. The test cell containing the liquid and gas mixture. Gravity is pointing in the negative z direction. The shape of the contact line reflects the curvature of the free surface.

The governing Eqs. (13), (16), and (18) are solved (simultaneously and iteratively) for the velocity $\mathbf{u}$, dynamic pressure p, and temperature T in both the liquid and gas domain separately subject to the boundary conditions at the interface and the inner surface of the solid walls. In addition, the governing Eq. (11) is solved for the concentration c_v in the gas phase subject to global mass conservation constraints (21).

The boundary conditions summarized in Table 1 are updated at each time step on both the liquid and the gas side of the interface, as well as the inner surfaces of solid walls. The nonlinear equations representing the boundary conditions at the interface are coupled and also need to be solved simultaneously. In particular, the interfacial fields j_v, T_i, and T_s are obtained by solving the system of Eqs. (22), (26), and (38) using Newton iteration with the values of the fields at the previous iteration used as initial condition. After this, the boundary conditions for the velocity, temperature, and concentration are updated using the remaining boundary conditions.

We implemented the model numerically by adapting an open-source CFD package OpenFOAM [31]. In the numerical solution procedure, each time step involves three major parts: (i) updating the interface shape and the computational mesh; (ii) updating the boundary conditions on the velocity, pressure, temperature, and concentration fields on both sides of the interface and the inner surfaces of solid walls; and (iii) updating pressure, velocity, temperature, and concentration fields in the bulk. In particular, pressure and velocity are solved for using PISO (Pressure Implicit with Splitting of Operators) algorithm [32], where the velocity field is predicted before the pressure equation is solved, so that the continuity (incompressibility) condition is satisfied, and velocity is then corrected based on changes in pressure field. It is an iterative procedure repeated until both the pressure and the velocity field converge. Once the velocity field has been computed, the temperature and concentration fields are updated. Since the shape of the interface, the boundary conditions, and the bulk fields are coupled, these three parts are repeated iteratively, until convergence.

Additional details can be found in Chapter 2 and the Appendices of Ref. [33]. The numerical codes and sample case files can be downloaded from https://github.com/tongran-qin/simple-fluid.

3. Results

To validate the generalized two-sided transport model described here, we implemented it numerically and reproduced several key results obtained previously for the well-studied problem [34,16,17,3] of buoyancy-thermocapillary-driven flow of volatile silicone oil (hexamethyldisiloxane) confined in a sealed rectangular test cell made of quartz (fused silica). The inner dimensions of the test cell are $L \times H \times W = 48.5$ mm $\times 10$ mm $\times 10$ mm and all material parameters of the fluid and its vapor can be found in Ref. [17].

A horizontal temperature gradient is applied by keeping the outer surfaces of the end walls at the temperatures $T_c = T_0 - \Delta T/2$ and $T_h = T_0 + \Delta T/2$. For comparison with the previous numerical studies, the same average thickness of the liquid layer $d_l = 2.5$ mm (which corresponds to the dynamic Bond number $Bo_D = O(1)$) and contact angle of 50° were used. While the numerical implementation of the model can describe flows in either 2D or 3D geometry, the results presented here were obtained exclusively for 2D flows (where the variation as well as the flow in the y-direction are neglected).

3.1. Dilute limits

Previous numerical studies [16,17] used transport models that were only justified in the limiting cases where the gas phase is

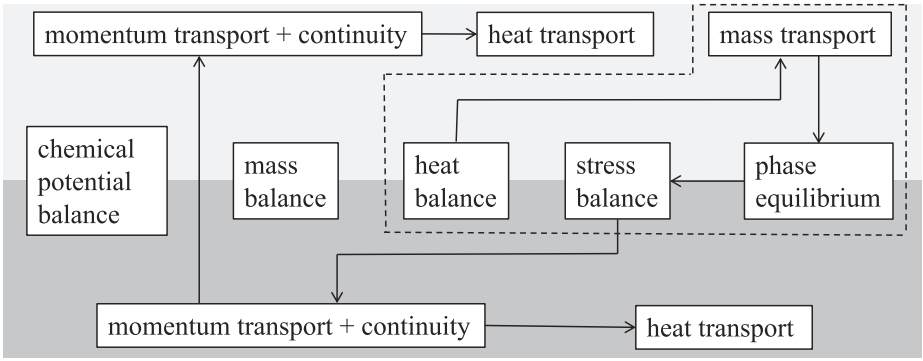

Fig. 2. The diagram showing the transport equations in the gas phase (light gray), liquid phase (dark gray), and the boundary conditions at the interface. The flowchart shows the order in which equations are solved in the simplified description of the problem, with the dashed box indicating the parts of the simplified model considered in this paper.

Table 1
Types of boundary conditions imposed on various boundaries in the numerical implementation of the model.

Field	Types of boundary conditions			
	Interface, gas side	Interface, liquid side	Hot/Cold walls	Other walls
u	Dirichlet	Neumann	Dirichlet	Dirichlet
p	Neumann	Dirichlet	Neumann	Neumann
T	Dirichlet	Neumann	Neumann	Neumann
c_v	Neumann	–	Neumann	Neumann

dominated by either vapor or air. In these limits the predictions of the present model should agree with those older models, and in fact this is what we find. Fig. 3 shows the asymptotic states of the flow (after initial transients have died down) for $T_0 = 293$ K and $\Delta T = 4$ K at the average air concentration $\bar{c}_a = 0.01$ (when the vapor is dominant) and $\bar{c}_a = 0.96$ (atmospheric conditions, when the air is dominant). This temperature difference was chosen since it corresponds to steady flows for the entire range of $\bar{c}_a$, as we show in the next Section. Although the shape of the streamlines depends on the (arbitrary) choice of the streamfunction values, the flow patterns produced using different transport models are found to be essentially indistinguishable in both limits.

A more quantitative comparison in terms of the interfacial mass flux J_v describing phase change, interfacial temperature profile T_i which controls the thermocapilllary stresses, and the resulting interfacial flow velocity u_i is provided in Fig. 4. Again, we find the predictions of the present model to be quite similar to those of the previous studies at $\Delta T = 4$ K. (We have also performed comparison for $\Delta T = 10$ K and found reasonable agreement, although direct comparison is more difficult due to time-dependence of the flow.) The slight discrepancy in u_i observed near the cold end of the test cell is due to the difference in the treatment of the gradient of the number density at the interface between the two models. The previous models [16,17], which rely on local mass conservation of the dilute component, lead to the following relation between the mass fractions of vapor and air

$$\frac{\partial_n \rho_v}{M_v} + \frac{\partial_n \rho_a}{M_a} = -\frac{p_g}{RT_i^2}\partial_n T. \tag{42}$$

The current formulation uses molar fractions instead, where (12) yields instead

$$\partial_n c_v + \partial_n c_a = 0. \tag{43}$$

The two relations become formally equivalent only when the gradient of T (or n_g) normal to the interface vanishes. When the gradient is not too large, the difference is quite small, so both models can be considered to provide a comparably accurate description of transport.

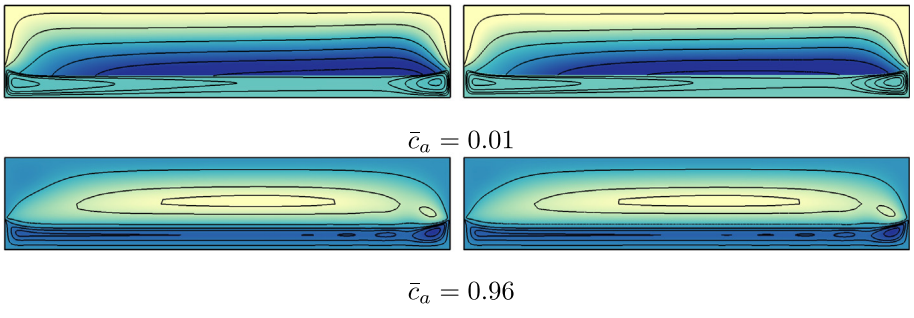

Fig. 3. Numerical results for the flow field at $\Delta T = 4$ K with different average concentrations of air $\bar{c}_a$ using the new (general) model (left column), and the previous (limiting-case) models [16,17] (right column). The cold end wall is on the left. Solid lines represent the streamlines of the flow. Here and below, the background represents the value of the stream function ψ, where darker (lighter) shade indicates higher (lower) values of ψ.

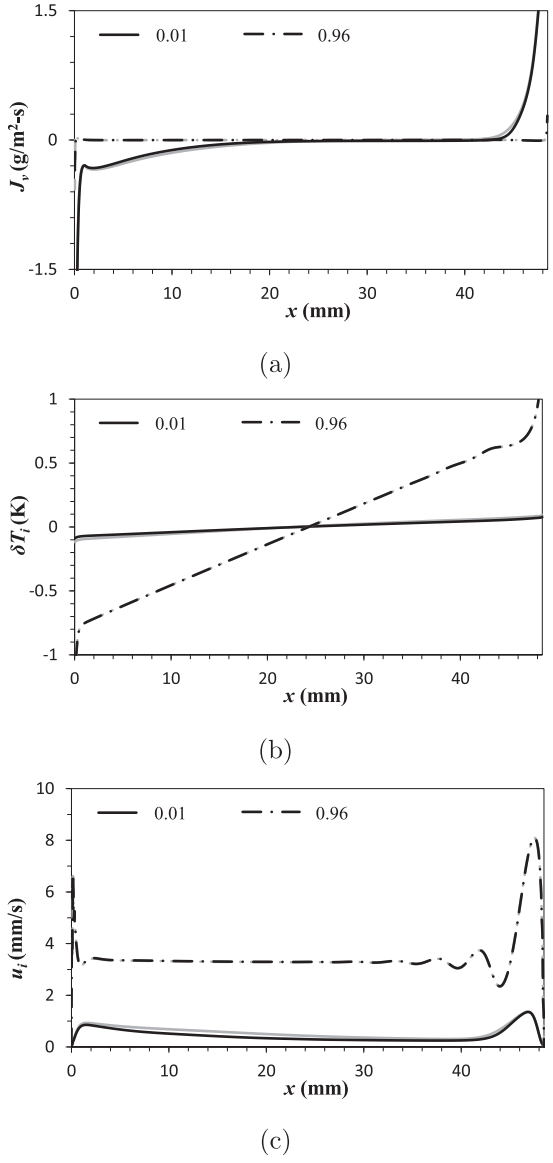

Fig. 4. Numerical results for the mass flux due to phase change (a), interfacial temperature profile (b), and the magnitude of the interfacial velocity (c) at $\Delta T = 4$ K at different average concentrations of air $\bar{c}_a$. To highlight the variation of the mass flux J_v and the interfacial temperature T_i in the central region of the cavity, the y-axis is truncated in (a) and (b), respectively. In addition, the deviation $\delta T_i = T_i - \langle T_i \rangle_x$ from the average is plotted in (b). Black lines represent the results based on the current model, grey lines – the results based on the previous models [?,17].

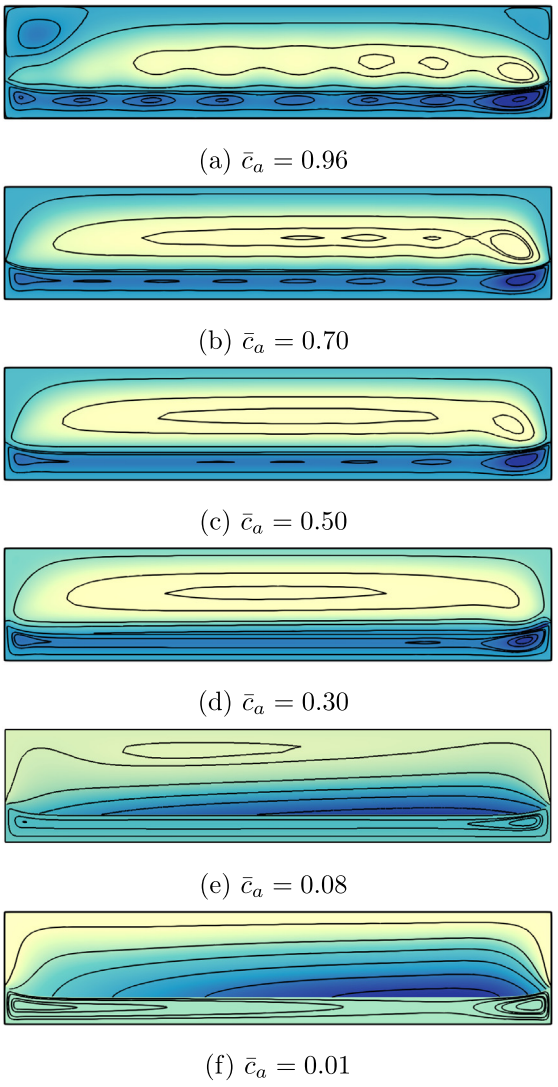

Fig. 5. Numerical results for the flow field at $\Delta T = 10$ K. The cold end wall is on the left. Solid lines represent the streamlines of the flow; color corresponds to the values of stream function ψ, where darker (lighter) indicates higher (lower) values of streamfunction ψ.

3.2. Flow regimes

Having validated the generalized transport model, we next investigate the effect of air on the convective flow over the entire range of $\bar{c}_a$, which was previously inaccessible to numerical simulations. Most of the results presented correspond to the imposed temperature difference of $\Delta T = 10$ K, to enable comparison with previous studies. Another advantage of this choice is that, as $\bar{c}_a$ varies between the two limits, the flow exhibits all the qualitatively different regimes observed previously at $Bo_D = O(1)$, with the corresponding flow states shown in Fig. 5. At atmospheric conditions (cf. Fig. 5(a)), we find an oscillatory multicellular flow (OMC) with the convection rolls covering the entire liquid layer. As $\bar{c}_a$ is decreased, the flow becomes steady and a steady multicellular (SMC) convection pattern is found (cf. Fig. 5(b)) with convection rolls still covering the entire liquid layer but becoming noticeably weaker. As $\bar{c}_a$ is decreased further (cf. Fig. 5(c–d)), the convection rolls in the liquid layer further weaken and start to disappear near the cold end, but persist near the hot end; the resulting state is referred to as the partial multicellular (PMC) pattern. At even lower $\bar{c}_a$ (cf. Fig. 5(e–f)), convection rolls in the bulk of the liquid layer disappear completely. This pattern is known as a steady unicellular flow (SUF) and features only a pair of weak convection rolls driven by buoyancy, one near each end wall.

The presence of air also strongly affects the flow in the gas phase. At relatively high $\bar{c}_a$, phase change is greatly suppressed and the flow in the gas phase is similar to that in the liquid (cf. Fig. 5(a)), with convection rolls appearing at almost the same positions along the interface, but rotating in the opposite direction. As $\bar{c}_a$ decreases, the convection rolls gradually weaken and disappear, also starting near the cold end (cf. Fig. 5(b-c)). At $\bar{c}_a \lesssim 0.3$, phase change becomes stronger, as indicated by the streamlines that originate and terminate at the interface (cf. Fig. 5(d-e)). For ever lower $\bar{c}_a$ (cf. Fig. 5(f)) all recirculation zones in the gas phase disappear, and the flow becomes uni-directional, from the hot side,

where the liquid evaporates, to the cold side, where the vapor condenses.

The different regimes are summarized in the flow regime map presented in Fig. 6 as a function of the average air concentration $\bar{c}_a$ and the interfacial Marangoni number

$$Ma_i = \frac{\gamma d_l^2}{\mu_l \alpha_l} \bar{\tau}. \tag{44}$$

Here $\bar{\tau}$ is the spatial average of the interfacial temperature gradient $\tau = \nabla_s T_i$, which reflects the imposed temperature difference. As the Figure illustrates, the flow regimes found in the simulations based on the generalized transport model are found to be in good agreement with both the experimental observations [25] and the predictions of the linear stability analysis [35], except at $\bar{c}_a \lesssim 0.2$ (the reasons for the discrepancy will be discussed later). Note that for the lower temperature difference $\Delta T = 4$ K the flow remains either in the SUF regime or in the PMC regime which is fairly similar. In both reigmes convection is suppressed throughout most of the cell.

4. Simplified transport model

In this section we will use the insight provided by the numerical simulations to derive a simplified transport model capable of providing a quantitative description of the flow in the SUF regime. The simplified description relies on the same governing equations, but makes certain reasonable assumptions that allow some variables to be decoupled, which allows the problem to be solved sequentially. The dashed box in Fig. 2 describes the part of the model treated in this paper and the arrows show the order in which various governing equations can be solved to determine all of the unknown fields.

The previous analysis of the $\bar{c}_a \to 0$ limit [17] has shown that it is the concentration field in the gas phase that ultimately plays the dominant role in this problem: it determines the interfacial temperature, surface stresses, and hence the flow field. As we will show below, a pretty accurate analytical description of the concentration field can be obtained for the base flow over the entire range of $\bar{c}_a$ in the central region of the flow, where the interface is nearly flat. The original analysis assumed that phase change and advection in this region are negligible to compute the concentration field $c_v = c_v(x)$. Why and under which conditions this result is valid will be discussed below.

4.1. Concentration profile in the gas phase

Following Ref. [36], we will introduce the rescaled coordinates $\chi = x/d_g$ and $\zeta = z/d_g$, where $d_g = H - d_l$ is the thickness of the gas layer in the central region. If we assume the interface coincides with the plane $z = 0$, then the gas phase corresponds to $0 < \zeta < 1$ and $0 < \chi < \Gamma_g$, where $\Gamma_g = L/d_g$ is the aspect ratio of the gas layer. Since the flow field is constrained to the $\chi - \zeta$ plane and is incompressible, it can be written in terms of the stream function $\psi(\chi, \zeta)$,

$$\mathbf{u}_g = \hat{\mathbf{x}}\partial_\zeta \psi - \hat{\mathbf{z}}\partial_\chi \psi. \tag{45}$$

As Fig. 4(a) illustrates, phase change in the central region is indeed negligible in the SUF regime. Hence, for a sufficiently large Γ_g (in this study $\Gamma_g \approx 6.5$), the flow of gas in this region can be assumed horizontal

$$\mathbf{u}_g = u_x \hat{\mathbf{x}} + u_z \hat{\mathbf{z}} \approx u_x \hat{\mathbf{x}}, \tag{46}$$

where $u_z/u_x = O\left(\Gamma_g^{-1}\right)$. We can therefore simplify the mass transport Eq. (11) to read

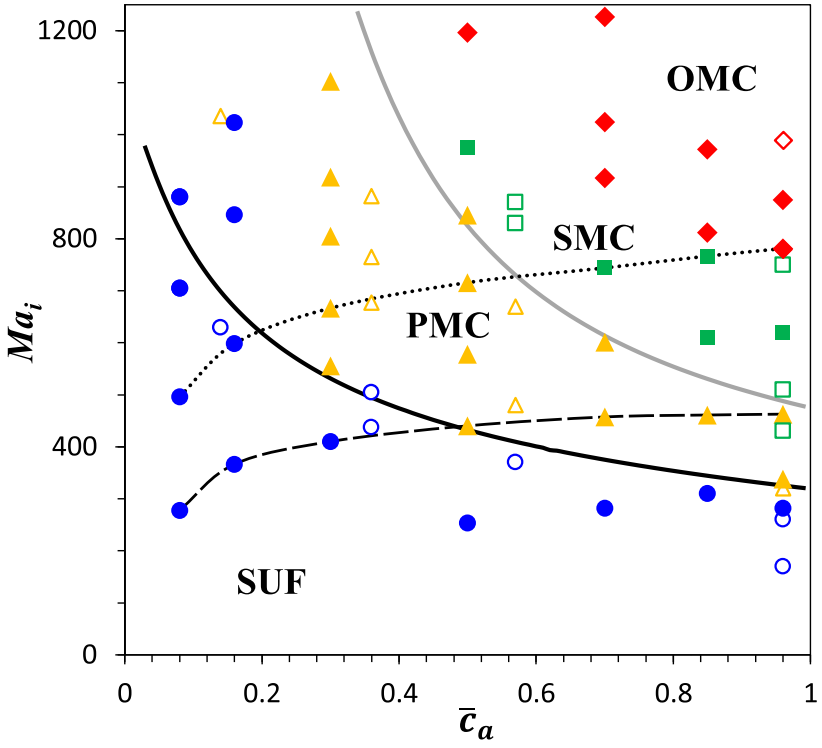

Fig. 6. Flow regime diagram in the $\bar{c}_a - Ma_i$ parameter space: SUF (○), PMC (△), SMC (□), and OMC (◇). Open symbols correspond to experimental results of Li et al. [25] and filled symbols – numerical results obtained in this study. Thick solid lines represent the critical Marangoni number for onset of the PMC (black) and SMC (dark grey) predicted by the linear stability analysis [35]. Thin dotted (dashed) black line corresponds to $\Delta T = 10$ K ($\Delta T = 4$ K).

$$d_g u_x \partial_\chi c_v = D\left(\partial_\chi^2 c_v + \partial_\zeta^2 c_v\right), \tag{47}$$

with the vertical component u_z of the velocity yielding a higher order correction. Furthermore, the horizontal component of velocity u_x can be decomposed into two contributions:

$$u_x = \bar{u}_x + \tilde{u}_x(\chi, \zeta), \tag{48}$$

where $\bar{u}_x = \text{const} < 0$ represents the mean flow (the vapor flows in the direction opposite to the applied temperature gradient) and $\tilde{u}_x$ represents the zero-mean recirculation flow such that

$$\int_0^1 \tilde{u}_x d\zeta = 0. \tag{49}$$

Correspondingly, we can write

$$\psi = \bar{u}_x \zeta + \tilde{\psi}(\zeta) + O\left(\Gamma_g^{-1}\right), \tag{50}$$

where $\tilde{u}_x = \partial_\zeta \tilde{\psi}$ and

$$\int_0^1 \partial_\zeta \tilde{\psi} d\zeta = \tilde{\psi}(1) - \tilde{\psi}(0) = 0. \tag{51}$$

Since the phase change at the liquid–gas interface is negligible in the central region, the mass/number flux vanishes, i.e., $\partial_\zeta c_v = 0$, at both $\zeta = 0$ and $\zeta = 1$. The solution obtained in Ref. [17] can be reproduced by setting $u_x = \bar{u}_x$ (i.e., $\tilde{u}_x = 0$) and solving (47) subject to the no-flux boundary conditions on c_v, which yields

$$c_v = C_0 + C_1 e^{-Pe_m \chi}. \tag{52}$$

Here

$$Pe_m = \frac{|\bar{u}_x| d_g}{D} \tag{53}$$

is the Péclet number which corresponds to the mean flow and C_0 and C_1 are the constants which can be determined based on the net amount of vapor and the net mass flux associated with phase change (to be determined later). In the general case (i.e., $\tilde{u}_x \neq 0$), the solution to (47) is

$$c_v = C_0 + C_1 e^{-Pe_m \chi}[1 + g(\zeta)], \tag{54}$$

where the function $g(\zeta)$ describing the vertical concentration profile satisfies the differential equation

$$g''(\zeta) = \frac{\bar{u}_x \tilde{u}_x(\zeta) d_g^2}{D^2}[1 + g(\zeta)]. \tag{55}$$

The right-hand-side of (55), and hence $g(\zeta)$ itself, is of order $\epsilon = Pe_m Pe_r$, where

$$Pe_r = \max_\zeta \frac{|\tilde{u}_x(\zeta)| d_g}{D} \tag{56}$$

is the Péclet number describing the strength of the recirculation flow $\tilde{u}_x$. To leading order in ϵ, we find

$$g(\zeta) = \frac{\bar{u}_x d_g^2}{D^2} \int \tilde{\psi}(\zeta) d\zeta + O(\epsilon^2). \tag{57}$$

The no-flux boundary conditions for c_v require $g'(0) = g'(1) = 0$. This is only consistent with (57) when (51) is satisfied, which justifies the separation of the flow field into the two components, $\bar{u}_x$ and $\tilde{u}_x$.

As long as $\epsilon \ll 1$, the variation of c_v in the vertical direction is negligible and the general solution (54) reduces to the special case (52). The crucial observation is that, although Pe_r can become quite large for $\bar{c}_a \to 1$, ϵ remains small regardless of the average concentration $\bar{c}_a$ of air for sufficiently low ΔT, as Fig. 7 illustrates. Indeed, numerically computed solutions for all $\bar{c}_a$ are characterized by concentration field (cf. Fig. 8) whose gradient in the vertical direction is small compared with that in the horizontal direction in the central region of the test cell. The variation in the vertical direction becomes more pronounced only for $\bar{c}_a \to 1$, where ϵ becomes comparable to unity and one has to use the solution (54) rather than (52). Moreover, at $\bar{c}_a = 0.96$ and the higher $\Delta T = 10$ K, where a strong convective pattern is present, one finds the concentration profile deviating near the interface from the solution (54) derived for the SUF regime, since phase change in the central region can no longer be neglected.

4.2. Net heat and mass flux

In order to compare the analytical predictions with numerical results quantitatively, we need to determine the mean flow velocity in the gas, which is related to the net mass flux. Since mass transport is essentially one-dimensional in the central region, the fluxes of vapor and air satisfy

$$\begin{aligned} J &= m_v^1 n_g (D\partial_x c_v - \bar{u}_x c_v), \\ 0 &= m_a^1 n_g (D\partial_x c_a - \bar{u}_x c_a), \end{aligned} \tag{58}$$

where J is the mean mass flux of vapor through a vertical cross-section. Adding these two equations and using the relation between c_a and c_v we find

$$\bar{u}_x = -\frac{J}{m_v^1 n_g}. \tag{59}$$

Using mass conservation, the mean mass flux at location x, $J_g(x)$, can be approximated by integrating the local mass flux J_v describing phase change at the interface, from x to L:

$$J_g(x) = \frac{1}{d_g} \int_x^L J_v(x')\, dx'. \tag{60}$$

Since evaporation (condensation) takes place mainly near the hot (cold) wall, mean flux is a function of x, however, as suggested by the numerical results, it becomes essentially constant $J_g(x) \approx J_0$ in the central region of the cell (cf. Fig. 9), where we have defined the characteristic mean mass flux

$$J_0 = \max_x J(x). \tag{61}$$

We will therefore use J_0 in place of J in (58) and (59).

Let us next consider the dependence of the mean flux J_0 on the average concentration of air $\bar{c}_a$. For sufficiently low ΔT and highly volatile fluids, the overall heat transport between the end walls is dominated by the latent heat associated with phase change, and the heat flux balance gives

$$J_0 \mathscr{L} = \frac{\Delta T}{Z_T}, \tag{62}$$

where

$$Z_T = Z_o + Z_d, \tag{63}$$

is the net thermal resistance, Z_o is the thermal resistance due to conduction through the end walls and the liquid wedges between the wall and the interface, and Z_d is the diffusive resistance of the gas layer [36]. While Z_o can be considered independent of the air concentration, Z_d depends sensitively on $\bar{c}_a$.

Since heat flows though the end walls and the liquid wedges between the wall and the interface sequentially, Z_o is a sum of the conduction resistances of the end walls $Z_w = \delta_w / k_w$ and the conduction resistances of the liquid wedges $Z_l \approx 0.5 d_l / k_l$, yielding

$$Z_o = 2(Z_w + Z_l) \approx 2\frac{\delta_w}{k_w} + \frac{d_l}{k_l}. \tag{64}$$

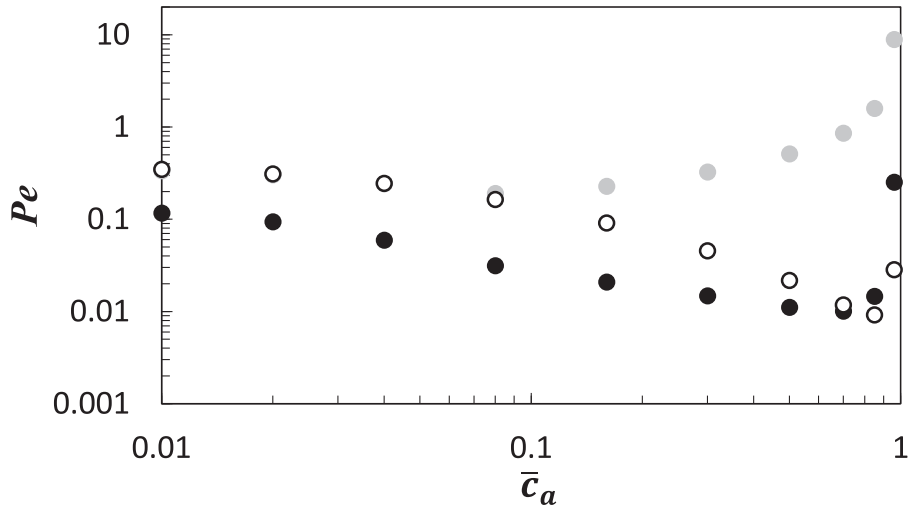

Fig. 7. The numerical values of Pe_m (open symbols), Pe_r (gray symbols), and their product ϵ (black symbols) at $\Delta T = 10$ K.

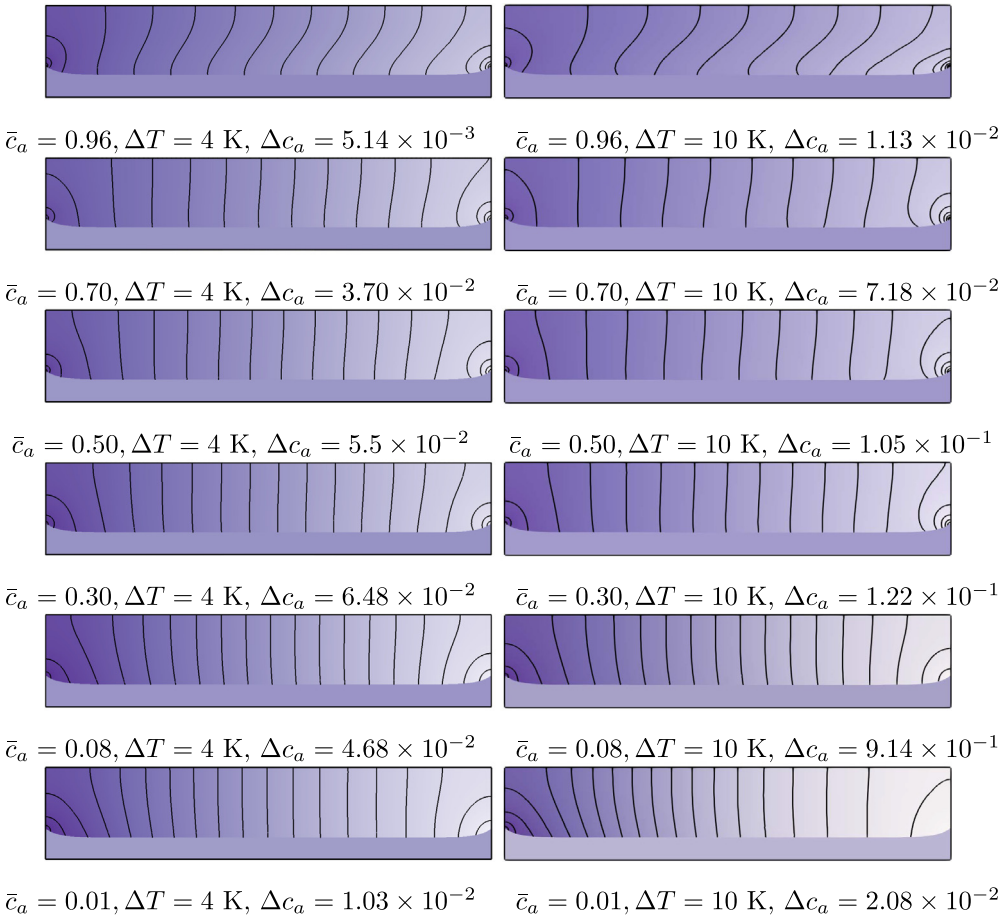

Fig. 8. Numerical results for the concentration of air $c_a = 1 - c_v$ in the gas phase for different $\bar{c}_a$ at $\Delta T = 4$ K (left column) and 10 K (right column). Solid lines represent twenty equally spaced level sets of the concentration field. In the gas phase, darker background indicates higher air concentration, while in the liquid phase the concentration field is undefined.

To determine Z_d, we solve the system of Eqs. (58) together with (59), which yields

$$J_0 = \frac{m_v^1 n_g D}{c_a} \partial_x c_v. \tag{65}$$

For volatile fluids, T_i is very close to T_s [19], so the concentration and temperature profiles are related. The phase equilibrium condition (23) can be expressed in terms of the concentrations using the relation

$$\frac{p_v}{p_v^0} = \frac{c_v}{\bar{c}_v}, \tag{66}$$

where $\bar{c}_v = 1 - \bar{c}_a$, such that

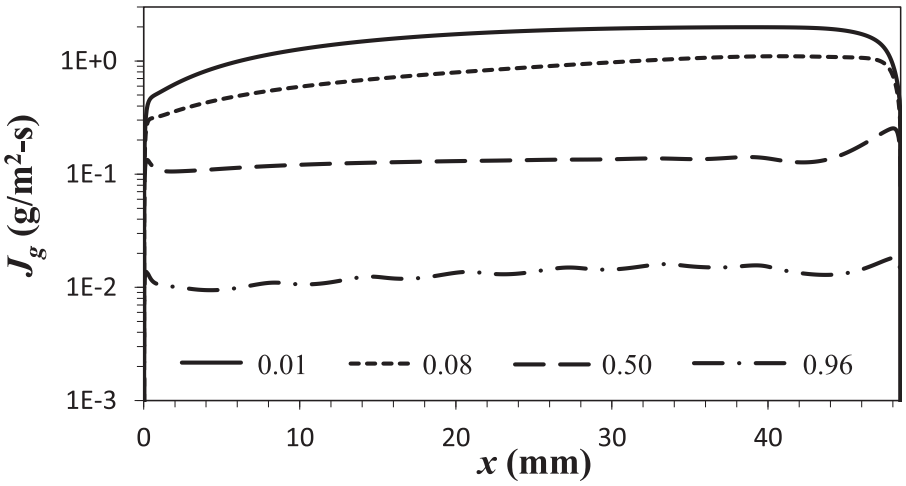

Fig. 9. Mean mass flux $J_g(x)$ in the gas phase (60) across the vertical cross-section of the cavity at location x. The value is computed numerically at $\Delta T = 10$ K with different average concentrations of air $\bar{c}_a$.

$$\frac{1}{T_i} = \frac{1}{T_0} - \frac{\overline{R}_v}{\mathscr{L}} \ln \frac{c_v}{\bar{c}_v} \tag{67}$$

and consequently

$$\partial_x c_v = -\partial_x c_a = \frac{\mathscr{L} c_v}{\overline{R}_v T_i^2} \tau, \tag{68}$$

where $\tau = \partial_x T_i$. Substituting the mean values for the concentrations and interfacial temperature into (68) and (65) yields

$$J_0 = \frac{1 - \bar{c}_a}{\bar{c}_a} \frac{m_v^1 n_g \mathscr{L} D}{\overline{R}_v T_0^2} \bar{\tau}, \tag{69}$$

where $\bar{\tau} = \Delta T'/L$ and $\Delta T' = T|_{x=L} - T|_{x=0}$ is the temperature difference between the inner surfaces of the hot and cold end walls. The heat flux balance at the interface near either of the end walls yields a relation similar to (62) which only includes the diffusive resistance

$$J_0 \mathscr{L} \approx \frac{\Delta T'}{Z_d}. \tag{70}$$

Solving (7), (69), and (70) together, we find

$$Z_d \approx \frac{\bar{c}_a}{1 - \bar{c}_a} \frac{\overline{R}_v^2 T_0^3 L}{D p_g \mathscr{L}^2}, \tag{71}$$

where $Dp_g = D_0 p_0$ is independent of $\bar{c}_a$ according to (5). This result corresponds to the effective condensation thermal conductivity $k_c = L/Z_d$ obtained by Peterson et al. [37].

4.3. Comparison of numerical and analytical results

With the solution for Z_o and Z_d, we can finally obtain the analytical estimate for J_0 using (62) and compare it with the numerical result for J_0, which is obtained using the numerical solution of local mass flux given by (60) and (61). Fig. 10 shows that the analytical and numerical results are in good agreement over the entire range of $\bar{c}_a$, suggesting that the one-dimensional description of transport in the gas phase is reasonably accurate. Note that at $\Delta T = 10$ K the flow is in the OMC regime at $\bar{c}_a = 0.96$ (cf. Fig. 6), so the predictions of our simplified transport model can be trusted far outside the SUF regime. As expected, the vapor flux is the largest when the air is removed entirely from the cell and $Z_d = 0$. An increase in $\bar{c}_a$ leads to an increase in Z_d and, correspondingly, a decrease in the vapor

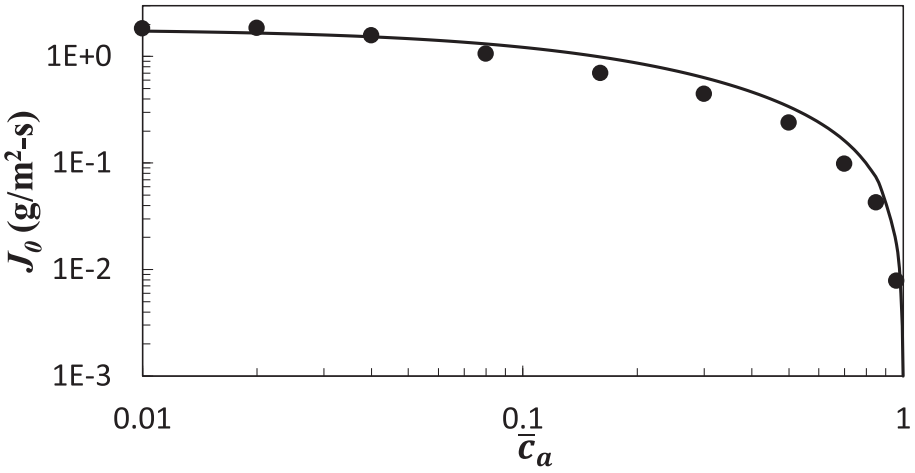

Fig. 10. Characteristic mass flux J_0 as a function of the average concentration of air $\bar{c}_a$ at $\Delta T = 10$ K. Solid line represents the analytical estimate based on (62), symbols – numerical results obtained using (60) and (61).

flux. The minor discrepancy between the numerical and analytical results is likely due to the contribution of heat conduction and advection in the liquid layer that have been ignored in our analysis of heat flux balance. These contributions are negligible for low $\bar{c}_a$, but would become progressively more important at higher $\bar{c}_a$, when phase change is suppressed, and our estimates of J_0 are expected to overestimate the numerical results, consistent with Fig. 10. In practical applications (*e.g.*, for heat pipes) the liquid layer will be substantially thinner, so conductive/convective heat flux would be negligible and the prediction of our simplified transport model would be even more accurate.

To compare the analytical prediction (52) for the concentration profiles with the numerical results, we need to determine the constants C_0 and C_1 in (52) or (54). When the concentration profile can be considered one-dimensional (i.e., for $\epsilon \ll 1$), the solution (52) can be obtained directly from the second of the two equations in (58) which yields

$$\partial_x c_a = -\frac{Pe_m}{d_g} c_a. \tag{72}$$

The average value of air concentration satisfies

$$\frac{1}{L}\int_0^L c_a dx = \bar{c}_a, \tag{73}$$

so that

$$c_a = 1 - c_v = \bar{c}_a \frac{Pe_m \Gamma_g e^{-Pe_m \chi}}{1 - e^{-Pe_m \Gamma_g}}. \tag{74}$$

Note that Pe_m can be computed from (53), (59), and (69) as long as the relation between $\bar{\tau}$ and ΔT is known.

As Fig. 11 illustrates, we find rather good agreement between the analytical predictions and the numerical results in the central region of the cavity. In the general case, the concentrations of both components in the gas mixture have an exponential profile. The concentration profiles become approximately linear only when $Pe_m \ll \Gamma_g^{-1}$. This limit corresponds to low values of the mean flow velocity $\bar{u}_x$ and hence low values of ΔT and/or high values of $\bar{c}_a$. In particular, for $\Delta T = 10$ K, we have $Pe_m < \Gamma_g^{-1}$ for $\bar{c}_a > 0.08$, and the concentration profiles indeed become essentially linear for $\bar{c}_a \gtrsim 0.08$ as shown in Fig. 11. The deviations noticeable at low $\bar{c}_a$ are mainly due to the breakdown of our assumption that phase change at the interface is negligible.

Substituting (72) into (68) and replacing T_i with T_0 we find

$$\tau = \frac{\overline{R}_v T_0^2}{d_g \mathscr{L}} \frac{Pe_m c_a}{1 - \bar{c}_a}. \tag{75}$$

This expression shows that the interfacial temperature profile is linear, quadratic, or exponential when the air concentration profile is constant, linear, or exponential, respectively. This is illustrated in Fig. 12, which shows that the analytical estimates for the interfacial temperature agree well with numerics. These results are in stark contrast with the very common assumption of linear temperature profile made in modeling heat pipes. While the temperature profile may indeed be linear in experiments with relatively small Γ_g and conducted at atmospheric pressure, the condition $Pe_m \ll \Gamma_g^{-1}$ will most certainly not be satisfied for high-aspect-ratio heat pipes operating at low $\bar{c}_a$, where the temperature profile will be exponential. Similarly, these results show the limitations of linear stability analysis of this flow [35] which assumed τ to be constant. In fact, the discrepancy between the numerical results and predictions of the linear stability analysis in this limit found in Fig. 6 are likely due in part to the deviation of τ from a constant. Another reason for the discrepancy is that the linear stability analysis breaks down at low $\bar{c}_a$ due to the wavelength of the instability becoming comparable to the system size L.

Whether the temperature profile is linear or not, the mean value of the interfacial temperature gradient can be found by substituting $c_a = \bar{c}_a$ into (75), which yields

$$\bar{\tau} \propto \frac{\bar{c}_a}{1 - \bar{c}_a} Pe_m = \frac{\bar{c}_a}{1 - \bar{c}_a} \frac{J_0 d_g}{m_v^1 n_g D} \propto \frac{\bar{c}_a}{1 - \bar{c}_a} J_0, \tag{76}$$

where $n_g D = p_g D/(\overline{R} T_0)$ is independent of $\bar{c}_a$ and J_0 can be obtained using the expression (62). At low air concentration, thermal resistance is dominated by the contribution Z_o, which is independent of $\bar{c}_a$. Hence J_0 is also independent of $\bar{c}_a$ and $\bar{\tau} \propto \bar{c}_a$. In particular, in the limit $\bar{c}_a \to 0$ we also have $\bar{\tau} \to 0$, consistent with our previous finding [19]. At high air concentration, thermal resistance is dominated by the contribution Z_d given by (71). Hence, $J_0 \propto (\Delta T/L)(1 - \bar{c}_a)/\bar{c}_a$, such that $\bar{\tau} \propto \Delta T/L$ is independent of $\bar{c}_a$. This is consistent with the results of both numerical simulations [17] and experiments [25] which found that the interfacial velocity (and hence thermocapillary stresses) remain essentially constant for $\bar{c}_a \gtrsim 0.14$.

Fig. 13 shows that at $\Delta T = 10$K, our theoretical predictions match the numerical results for the interfacial temperature gradient at low $\bar{c}_a$, but overestimate them at high $\bar{c}_a$. The reason is that at high ΔT, our assumption that conductive and especially convective heat transfer in the liquid layer is negligible, breaks down. Numerical simulations show that $\bar{\tau} \propto \Delta T/L$ only at sufficiently low ΔT. At higher ΔT we have [16]

$$\frac{\Delta T}{L} \approx \frac{1 + a\bar{\tau}^2}{1 + b\bar{\tau}^2} \bar{\tau} \geqslant \bar{\tau}, \tag{77}$$

where a and $b \leqslant a$ are parameters that dependent on $\bar{c}_a$ and the geometry of the liquid layer. In particular, the data in Fig. 13 corresponds to numerical simulations for $\Delta T = 10$ K, where strong convection in the (relatively thick) layer makes the relationship between $\bar{\tau}$ and $\Delta T/L$ nonlinear. For thin liquid layers characteristic of, *e.g.*, heat pipes, both conductive and convective heat transfer in the liquid phase can be ignored, so our theoretical description should be quite accurate over the entire range of $\bar{c}_a$.

In conclusion of this section, let us return to the issue of validity of the one-dimensional solution (52) for the concentration profile. The value of ϵ can be easily estimated in the practically important case $\bar{c}_a \to 0$. In this limit, the gas velocity is much larger than the liquid velocity, so the flow profile in the gas layer in the central region is nearly parabolic and symmetric about its mid-height, so $\max_\zeta |\tilde{u}_x| = |\bar{u}_x|$. Furthermore, diffusive resistance Z_d is negligible and, since the wall material (fused quartz) is a far better thermal conductor than the liquid (silicone oil), $Z_T \approx Z_o \approx d_l/k_l$. Substituting (59) and (62) into (53) and (56) we find

$$Pe_r = Pe_m = \frac{\Delta T d_g}{m_v^1 n_g D \mathscr{L} Z_T} \approx \frac{d_g}{d_l} \frac{\mu_l}{\mu_v} Sc_v E, \tag{78}$$

where $Sc_v = \nu_v/D$ is the Schmidt number for the vapor and

$$E = \frac{k_l \Delta T}{\mu_l \mathscr{L}} \tag{79}$$

is the evaporation number [38]. The analytical solution (52) provides a good approximation when $\epsilon \ll 1$, which is equivalent to

$$\Delta T \ll Sc_v^{-1} \frac{d_l}{d_g} \frac{\mu_v \mathscr{L}}{k_l} \approx 27 \text{ K}. \tag{80}$$

In particular, for $\Delta T = 10$ K, Eq. (78) yields $Pe_r = Pe_m = 0.37$, which is very close to the value (0.4) obtained numerically (cf. Fig. 7).

In the opposite limit (*e.g.*, at atmospheric conditions), diffusive resistance dominates, $Z_T \approx Z_d$, so with the help of (71) we find

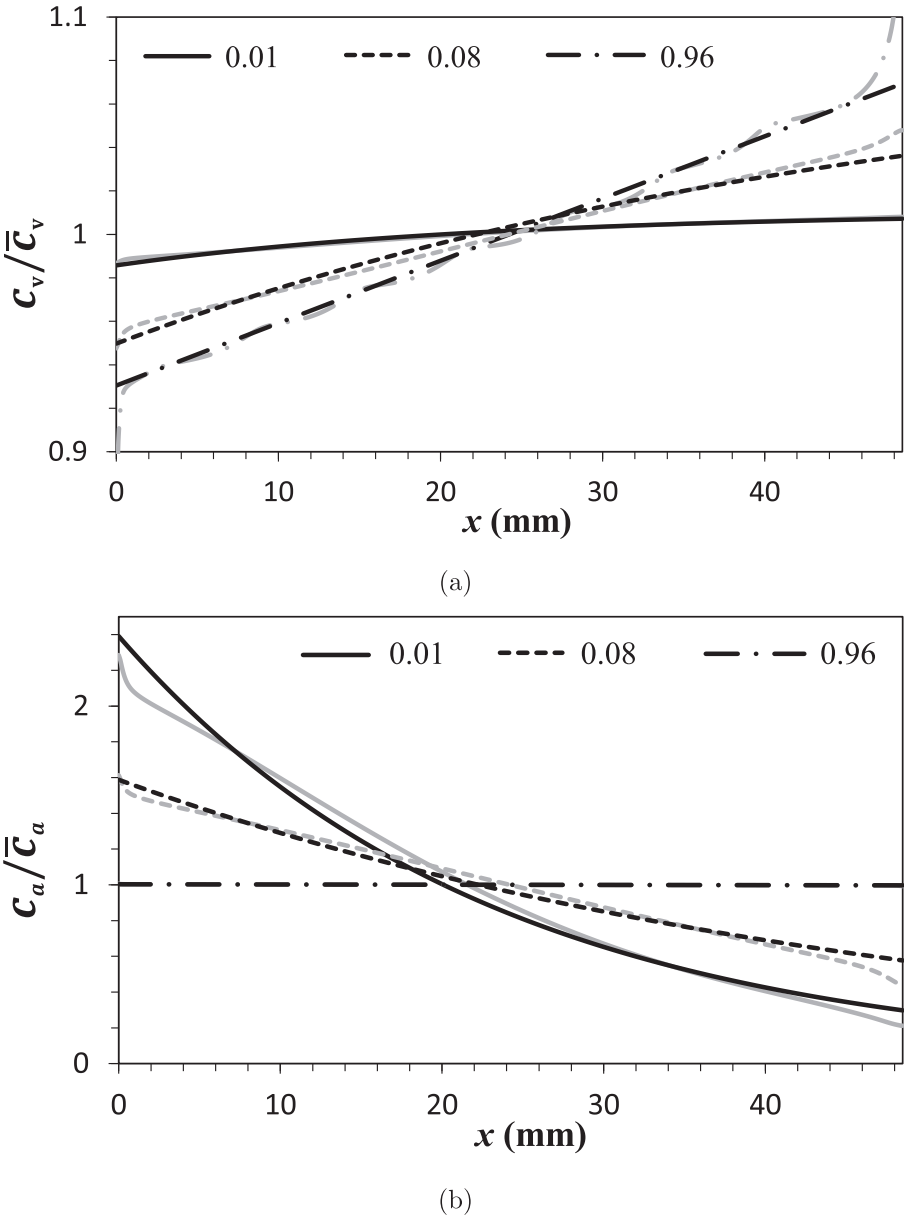

Fig. 11. Normalized concentration profiles in the gas phase at $\Delta T = 10$ K for vapor (a) and (b) air with different $\bar{c}_a$. Numerical and analytical results are represented by gray and black lines, respectively. Numerical results correspond to the mid-height of the gas layer.

$$Pe_m \approx \frac{\Delta T d_g}{\mathscr{L} Z_T} = \frac{1-\bar{c}_a}{\bar{c}_a} \frac{\mathscr{L}}{\bar{R}_v T_0} \frac{d_g}{L} \frac{\Delta T}{T_0}, \tag{81}$$

which, as Fig. 7 illustrates, vanishes as $\bar{c}_a \to 1$. The recirculation component of the flow in this limit can be estimated by balancing the viscous and thermocapillary stresses [17]

$$\max_\zeta \tilde{u}_x \approx \frac{1}{4} \frac{\gamma d_l}{\mu_l} \bar{\tau} \sim \frac{1}{4} \frac{\gamma d_l \Delta T}{\mu_l L}, \tag{82}$$

which yields

$$Pe_r \sim \frac{1}{4} \frac{\gamma d_l d_g \Delta T}{\mu_l L D} = \frac{1}{4} \frac{1}{1-\bar{c}_a} \frac{\gamma d_l d_g \Delta T p_v^0}{\mu_l L D_0 p_0}. \tag{83}$$

As our estimate shows and numerical data presented in Fig. 7 confirms, Pe_r diverges at $\bar{c}_a \to 1$, however the product of the two Peclet numbers approaches a constant

$$\epsilon \sim \frac{1}{4} \frac{\gamma d_l \mathscr{L}}{\mu_l \bar{R}_v D_0} \frac{p_v^0}{p_0} \frac{d_g^2}{L^2} \frac{\Delta T^2}{T_0^2}. \tag{84}$$

In particular, we find that $\epsilon \ll 1$ when

$$\Delta T \ll 2 \frac{L}{d_g} \left[\frac{\mu_l \bar{R}_v D_0}{\gamma d_l \mathscr{L}} \frac{p_0}{p_v^0} \right]^{1/2} T_0 \approx 34 \text{ K}. \tag{85}$$

Note that the estimate (82) and hence (83) and (85) is conservative since, for $\Delta T \gtrsim 10$ K, the interfacial temperature gradient $\bar{\tau}$ is only a fraction of $\Delta T/L$ (a third to a quarter for $\bar{c}_a = 0.96$ [16]).

To sum up, for the silicone oil studied here, our estimates suggest that the one-dimensional approximation (52) should hold for any $\bar{c}_a$ as long as ΔT is around 10 K or less; the more general expression (54) has to be used for larger temperature gradients. Indeed, our numerical simulations show that the concentration profile develops noticeable variation in the vertical direction only for $\Delta T \gtrsim 10$ K. For comparison, the onset of convection pattern

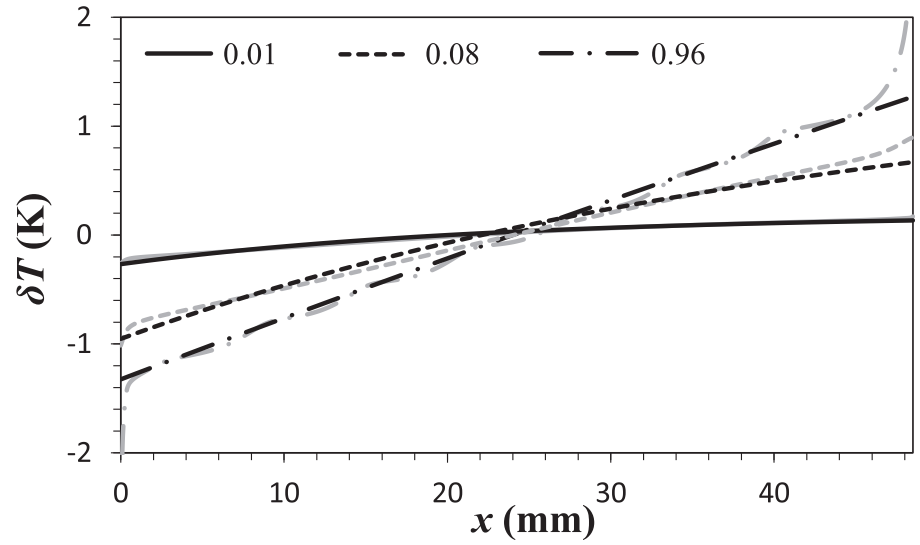

Fig. 12. Interfacial temperature at $\Delta T = 10$ K with different $\bar{c}_a$. The variation $\delta T_i = T_i - T_0$ about the mean is plotted. Numerical and analytical results are represented by gray and black lines, respectively.

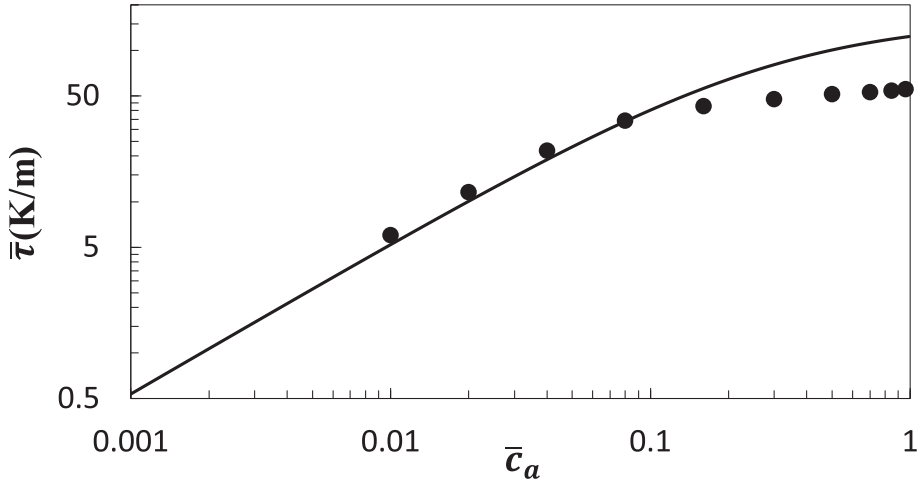

Fig. 13. The mean value of the interfacial temperature gradient $\bar{\tau}$ as a function of the average air concentration $\bar{c}_a$ at $\Delta T = 10$ K. Numerical and analytical results are represented by solid line and symbols, respectively.

(SMC regime) at atmospheric conditions corresponds to $\Delta T \approx 4$ K in this geometry [16,25]. It should be noted that some of our assumptions (most notably, that phase change at the interface is negligible) start to break down when convection pattern develops, which leads to spatial modulation developing on top of the (nearly linear) interfacial temperature profile (see, e.g., Fig. 5 in Ref. [16]).

5. Summary

We have formulated and implemented numerically a generalized two-sided transport model for two-phase flow of nonisothermal volatile fluids which accounts for momentum, mass, and heat transport in both phases, as well as phase change at the liquid-gas interface. The model is valid for arbitrary composition of the gas phase, described in terms of the average concentration of air $\bar{c}_a$ here. It has been thoroughly validated by comparing its predictions both against other numerical models in the limiting cases $\bar{c}_a \to 1$ and $\bar{c}_a \to 0$ and against experimental observations [25] and linear stability analysis [35] over the entire range of $\bar{c}_a$,. The model has been used to study the flow of low viscosity silicone oil confined in a sealed cavity and driven by a horizontal temperature gradient. In particular, we have investigated how the flow changes when the pressure inside the cavity, and with it the composition of the gas layer, changes. Numerical simulations reported here and elsewhere [16,19,17] show that the flow in both layers is very different in the limits $\bar{c}_a \to 0$ and $\bar{c}_a \to 1$.

In order to understand these differences, we have developed a simplified transport model for the central region of the cavity which showed that, somewhat surprisingly, for $\bar{c}_a \neq 0$, it is the gas layer that controls the flow in the liquid layer. More specifically, mass transport in the gas layer determines its local composition, the interfacial temperature, and hence the thermocapillary stresses which drive the flow in the liquid layer. Quite interestingly, we found that, in high-aspect ratio geometries (such as the interior of a heat pipe), the mass transport in the gas layer remains diffusion-dominated and hence independent of the flow, even in the limit when the traditionally defined Peclet number, which corresponds to our Pe_r, becomes large compared to unity. We have shown that mass transport is in fact described by two different

Peclet numbers – Pe_r which describes recirculation, and Pe_m which describes the mean flow – and that it is the product $\epsilon = Pe_r Pe_m$ that controls whether mass transport in the gas phase is dominated by diffusion or advection. We have also shown that, for small to moderate imposed temperature gradients, ϵ remains small regardless of the composition of the gas phase.

Our simplified transport model has not just qualitatively explained a range of numerical and experimental results, it was also found to be capable of producing quantitatively accurate predictions. For instance, it correctly predicted the concentration profile in the gas phase and the interfacial temperature profile over the entire range of $\bar{c}_a$. In particular, we found that the interfacial temperature profile is generally exponential, not linear as assumed by many one-sided transport models of two-phase flows. The assumption of linearity can be justified in the limit $\bar{c}_a \to 1$ (*e.g.*, at atmospheric conditions), but not in the practically important limit $\bar{c}_a \to 0$. Furthermore, the model correctly predicted the dependence of the net vapor flux (and hence the net heat flux) and the average interfacial temperature gradient (and hence thermocapillary stress) on $\bar{c}_a$. Finally, it is worth pointing out that although the simplified transport model is formally valid only in the steady unicellular flow regime, it was found to give reasonably accurate predictions even when convection rolls appear.

Declaration of Competing Interest

There are no conflict of interest in this work.

Acknowledgements

This work has been supported by the National Science Foundation under Grant No. CMMI-1511470.

Appendix A. Supplementary material

Supplementary data associated with this article can be found, in the online version, at https://doi.org/10.1016/j.ijheatmasstransfer.2019.118934.

References

[1] A. Faghri, Heat Pipe Science And Technology, Taylor & Francis Group, Boca Raton, 1995.
[2] W. Minkowycz, E. Sparrow, Condensation heat transfer in the presence of noncondensables, interfacial resistance, superheating, variable properties, and diffusion, Int. J. Heat Mass Trans. 9 (1966) 1125.
[3] T. Qin, Buoyancy-Thermocapillary Convection of Volatile Fluids in Confined and Sealed Geometries, Ph.d. thesis, Georgia Institute of Technology, 2016.
[4] M.K. Smith, S.H. Davis, Instabilities of dynamic thermocapillary liquid layers. Part 1. Convective instabilities, J. Fluid Mech. 132 (1983) 119–144.
[5] M.K. Smith, S.H. Davis, Instabilities of dynamic thermocapillary liquid layers. Part 2. Surface-wave instabilities, J. Fluid Mech. 132 (1983) 145–162.
[6] D. Villers, J.K. Platten, Coupled buoyancy and Marangoni convection in acetone: experiments and comparison with numerical simulations, J. Fluid Mech. 234 (1992) 487–510.
[7] H. Ben Hadid, B. Roux, Buoyancy- and thermocapillary-driven flows in differentially heated cavities for low-Prandtl-number fluids, J. Fluid Mech. 235 (1992) 1–36.
[8] M. Mundrane, A. Zebib, Oscillatory buoyant thermocapillary flow, Phys. Fluids 6 (10) (1994) 3294–3306.
[9] X. Lu, L. Zhuang, Numerical study of buoyancy- and thermocapillary-driven flows in a cavity, Acta Mech. Sin. (Engl. Ser.) 14 (2) (1998) 130–138.
[10] V.S. Ajaev, G.M. Homsy, Steady vapor bubbles in rectangular microchannels, J. Colloid Interface Sci. 240 (2001) 259–271.
[11] V.M. Shevtsova, A.A. Nepomnyashchy, J.C. Legros, Thermocapillary-buoyancy convection in a shallow cavity heated from the side, Phys. Rev. E 67 (2003) 066308.
[12] M. Markos, V.S. Ajaev, G.M. Homsy, Steady flow and evaporation of a volatile liquid in a wedge, Phys. Fluids 18 (2006) 092102.
[13] J. Zhang, S.J. Watson, H. Wong, Fluid flow and heat transfer in a dual-wet micro heat pipe, J. Fluid Mech. 589 (2007) 1–31.
[14] T. Qin, R.O. Grigoriev, Convection, evaporation, and condensation of simple and binary fluids in confined geometries, in: Proc. of the 3rd Micro/Nanoscale Heat & Mass Transfer International Conference, MNHMT2012–75266, 2012.
[15] K. Kafeel, A. Turan, Axi-symmetric simulation of a two phase vertical thermosyphon using Eulerian two-fluid methodology, Heat Mass Transf. 49 (2013) 1089–1099.
[16] T. Qin, Z. Tuković, R.O. Grigoriev, Buoyancy-thermocapillary convection of volatile fluids under atmospheric conditions, Int. J. Heat Mass Transf. 75 (2014) 284–301.
[17] T. Qin, R.O. Grigoriev, The effect of noncondensables on buoyancy-thermocapillary convection of volatile fluids in confined geometries, Int. J. Heat Mass Transf. 90 (2015) 678–688.
[18] T. Qin, R.O. Grigoriev, The effect of noncondensables on buoyancy-thermocapillary convection in confined and volatile fluids, in: Proc. of 11th AIAA/ASME Joint Thermophysics and Heat Transfer Conference, AIAA Aviation and Aeronautics Forum and Exposition, AIAA2014-1898558, 2014.
[19] T. Qin, Z. Tuković, R.O. Grigoriev, Buoyancy-thermocapillary Convection of Volatile Fluids under their vapors, Int. J. Heat Mass Transf. 80 (2015) 38–49.
[20] R. Krishna, J. Wesselingh, The Maxwell-Stefan approach to mass Transf, Chem. Eng. Sci. 52 (6) (1997) 861–911.
[21] R.W. Schrage, A Theoretical Study of Interface Mass Transf, Columbia University Press, New York, 1953.
[22] G. Wyllie, Evaporation and surface structure of liquids, Proc. Roy. Soc. Lond. 197 (1949) 383–395.
[23] R. Rudolf, M. Itoh, Y. Viisanen, P. Wagner, Sticking probabilities for condensation of polar and nonpolar vapor molecules, in: N. Fukuta, P.E. Wagner (Eds.), Nucleation and Atmospheric Aerosols, A, Deepak Publishing, Hampton, 1992, pp. 165–168.
[24] A. Oron, S.H. Davis, S.G. Bankoff, Long-scale evolution of thin liquid films, Rev. Modern Phys. 69 (3) (1997) 931–980.
[25] Y. Li, R.O. Grigoriev, M. Yoda, Experimental study of the effect of noncondensables on buoyancy-thermocapillary convection in a volatile low-viscosity silicone oil, Phys. Fluids 26 (2014) 122112.
[26] J.C. Tannehill, D.A. Anderson, R.H. Pletcher, Computational fluid mechanics and heat Transf., Taylor & Francis, Washington, DC, second ed., ISBN 156032046X, 1997.
[27] J.H. Ferziger, M. Perić, Computational Methods for Fluid Dynamics, Springer, Berlin, 1997.
[28] R. LeVeque, Finite Volume Methods for Hyperbolic Problems, Cambridge University Press, Cambridge, 2002.
[29] H. Jasak, Z. Tuković, Dynamic Mesh Handling in OpenFOAM Applied to Fluid-Structure Interaction Simulations, in: Proceedings of the V European Conference on Computational Fluid Dynamics (ECCOMAS CFD), 2010.
[30] Z. Tuković, H. Jasak, A moving mesh finite volume interface tracking method for surface tension dominated interfacial fluid flow, Compu. Fluids 55 (2012) 70–84.
[31] http://www.openfoam.org
[32] R.I. Issa, Solution of the implicitly discretized fluid flow equations by operator-splitting, J. Comp. Phys. 62 (1986) 40–65.
[33] T. Qin, Buoyancy-Thermocapillary Convection of Volatile Fluids in Confined and Sealed Geometries, Springer Theses, Springer International Publishing, ISBN 9783319613314, 2017.
[34] Y. Li, M. Yoda, The wave length of the pattern for buoyancy-thermocapillary convection in 0.65 cSt silicone oil, private communication, 2015.
[35] R.O. Grigoriev, T. Qin, The effect of phase change on stability of convective flow in a layer of volatile liquid driven by a horizontal temperature gradient, J. Fluid Mech. 838 (2018) 248–283.
[36] J. Liu, R.O. Grigoriev, Analytical solution for filmwise condensation in confined high-aspect ratio geometry, Int. J. Heat Mass Transf. 133 (2019) 561–571.
[37] P.F. Peterson, V.E. Schrock, T. Kageyama, Diffusion layer theory for turbulent vapor condensation with noncondensable gases, J. Heat Transf.-Trans. ASME 115 (1993) 998–1003.
[38] J.P. Burelbach, S.G. Bankoff, S.H. Davis, Nonlinear stability of evaporating/condensing liquid films, J. Fluid Mech. 195 (1988) 463–494.